



SELECTING M GIANTS WITH INFRARED PHOTOMETRY: DISTANCES, METALLICITIES, AND THE SAGITTARIUS STREAM

JING LI^{1,2}, MARTIN C. SMITH¹, JING ZHONG¹, JINLIANG HOU¹, JEFFREY L. CARLIN³, HEIDI JO NEWBERG³, CHAO LIU⁴, LI CHEN¹, LINLIN LI¹, ZHENGYI SHAO¹, EMMA SMALL¹, AND HAO TIAN⁵

¹ Key Laboratory of Galaxies and Cosmology, Shanghai Astronomical Observatory, Chinese Academy of Sciences, 80 Nandan Road, Shanghai, 200030, China; lijing@shao.ac.cn, msmith@shao.ac.cn

² University of Chinese Academy of Sciences, 19A Yuquan Road, Beijing 100049, China

³ Department of Physics, Applied Physics and Astronomy, Rensselaer Polytechnic Institute, Troy, NY 12180, USA

⁴ Key Laboratory of Optical Astronomy, National Astronomical Observatories, Chinese Academy of Sciences, Datun Road 20A, Beijing 100012, China

⁵ Kapteyn Astronomical Institute, University of Groningen, P.O. Box 800, 9700 AV Groningen, The Netherlands

Received 2015 July 3; accepted 2016 February 26; published 2016 May 23

ABSTRACT

Using a spectroscopically confirmed sample of M giants, M dwarfs, and quasars from the LAMOST survey, we assess how well *Wide-field Infrared Survey Explorer (WISE)* and Two Micron All Sky Survey color cuts can be used to select M giant stars. The *WISE* bands are very efficient at separating M giants from M dwarfs, and we present a simple classification that can produce a clean and relatively complete sample of M giants. We derive a new photometric relation to estimate the metallicity for M giants, calibrated using data from the APOGEE survey. We find a strong correlation between the $(W1 - W2)$ color and $[M/H]$, where almost all of the scatter is due to photometric uncertainties. We show that previous photometric distance relations, which are mostly based on stellar models, may be biased and devise a new empirical distance relation, investigating trends with metallicity and star formation history. Given these relations, we investigate the properties of M giants in the Sagittarius stream. The offset in the orbital plane between the leading and trailing tails is reproduced, and by identifying distant M giants in the direction of the Galactic anticenter, we confirm that the previously detected debris in the outer halo is the apocenter of the trailing tail. We also find tentative evidence supporting an existing overdensity near the leading tail in the northern Galactic hemisphere, possibly an extension to the trailing tail (so-called Branch C). We have measured the metallicity distribution along the stream, finding a clear metallicity offset between the leading and trailing tails, in agreement with models for the stream formation. We include an online table of M giants to facilitate further studies.

Key words: galaxies: individual (Sagittarius) – Galaxy: halo – Galaxy: structure – stars: abundances – stars: distances – stars: late-type

Supporting material: machine-readable table

1. INTRODUCTION

Standard Λ CDM cosmology predicts that the stellar halo is formed by merger of smaller satellite systems. This process would leave its imprint in a diffuse stellar halo on a large scale. The density, luminosity, velocity, and metallicity of the stellar halo can thus provide direct constraints on the evolution history (e.g., Newberg et al. 2002, 2009; Rocha-Pinto et al. 2004; Belokurov et al. 2006; Smith et al. 2009; Schlafman et al. 2012; Drake et al. 2013). Therefore, detecting structures in the stellar halo of the Milky Way is particularly important for understanding the evolution of our Galaxy.

M giant stars, with temperatures in the range 2400–3700 K, are very bright; at the tip of the red giant branch (RGB), their luminosities are $\sim 10^3 L_{\odot}$, making them excellent tracers of substructures at large distances in the outer Galactic halo (e.g., Majewski et al. 2003; Sharma et al. 2010; Bochanski et al. 2014; Sheffield et al. 2014). However, only relatively metal-rich stellar populations in the RGB can extend to cool enough temperatures to produce M giants, making M giants a rare spectral type in the mostly metal-poor Galactic halo.

As M giants are useful for tracing metal-rich structures, they are ideal for tracing the Sagittarius (Sgr) stream. Since this stream is (relatively) metal-rich, it contains a significant number of M giants. Currently, M giants are mainly selected from multiband photometric surveys as spectral identification is

only available for small samples. From a near-infrared (NIR) color–color diagram of stars from the Two Micron All Sky Survey (2MASS) photometry catalog, Majewski et al. (2003), for the first time, selected thousands of M giant candidates that were used to map the all-sky view of the Sgr dwarf galaxy. Recently, Bochanski et al. (2014) used a combined NIR and optical color selection to assemble a catalog of 374 faint M giant candidates from the UKIRT Infrared Deep Sky Survey (UKIDSS) and the Sloan Digital Sky Survey (SDSS). These candidates were selected by position in the $(J - H)_0$ versus $(J - K)_0$ color–color diagram for point sources in UKIDSS. This NIR color–color selection is similar to that of Majewski et al. (2003), but slightly shifted toward to reduce contamination from bluer nearby M dwarfs. They used an NIR–optical $(g - i)_0$ versus $(i - K)_0$ color–color selection to identify quasar (QSO) contamination, removing nearly half of their M giant candidates. In order to further confirm those M giants, they have begun high-resolution spectroscopic follow-up observations. From their 16 M giant candidates, only 3 are confirmed to be genuine M giants, which implies that the efficiency of selecting true M giants is only $\sim 18\%$, although this is partially a consequence of operating at faint magnitudes where the fraction of M giants to M dwarfs drops dramatically. During the preparation of this paper, Koposov et al. (2015) showed that mid-IR photometry is more effective for

classification and used this technique to investigate Sgr debris toward the Galactic anticenter.

It is clear that M giant samples need to be enlarged, not only with respect to the number of candidates but also in the sky coverage. The selection efficiency also needs to be improved substantially. An important way to test and improve photometric selection techniques is through large spectroscopic surveys containing confirmed M giant stars. One such survey is the LAMOST Experiment for Galactic Understanding and Exploration (LEGUE). LAMOST (the Large sky Area Multi-Object fiber Spectroscopic Telescope, also known as the Guo Shou Jing Telescope) has been in full survey mode since 2012 (Luo et al. 2015). From the huge catalog of LAMOST spectra Zhong et al. (2015b, hereafter Z15; see also Zhong et al. 2015a) constructed M giant templates and identified around 9000 M giant stars, which is currently the largest spectroscopic catalog of M giants. This large spectroscopically selected catalog provides a mechanism with which we can explore more efficient multiband photometric methods for separating M giants from the much more numerous M dwarfs in the Milky Way.

The paper is arranged as follows. Section 2 briefly describes the LAMOST data we used in this work and the spectroscopic M giant/M dwarf identification. In Section 3 we recap previous methods for selecting M giants and introduce our new selection criteria based on IR photometry. In Section 4 we analyze the properties of these M giants, constructing photometric relations for estimating metallicities (Section 4.1) and distances (Section 4.2). In Section 5 we use our selection criteria to identify M giants from the all-sky ALLWISE database in order to study the Sgr stream. We give our conclusions in Section 6.

2. LAMOST DATA AND SPECTRAL CLASSIFICATION

In order to study the properties of M giants, we first need to identify a large sample of such stars. We do this using data from the LAMOST spectroscopic telescope (Zhao et al. 2012). LAMOST is a large-aperture (4–5 m) spectroscopic survey telescope, operated by the National Astronomical Observatories, Chinese Academy of Sciences. It has a total of 4000 fibers across a 20 deg² field of view. Since 2012 the telescope has been carrying out an extensive survey of stars in the Milky Way (Deng et al. 2012), obtaining spectra for over 1 million stars each year at a resolution of $R \approx 1800$. In general, the input catalog uses a selection method that either is random or preferentially selects less populous regions of color–magnitude space (Luo et al. 2015). Data Release 1 (DR1) was released to the international community in 2015 (Luo et al. 2015).

The survey has been shown to be extremely useful for obtaining large samples of red giant stars (notably the sample of K giants from Liu et al. 2014), but unfortunately the LAMOST pipeline has difficulties with cool M-type stars, in particular in the 2D spectral analysis and flux calibration (Luo et al. 2015). This leads to problems classifying late-type stars such as M giants owing to the numerous molecular bands that affect the morphology of the spectra.

To circumvent these problems, a separate analysis of the M-type stars needs to be undertaken. For example, Yi et al. (2014) applied a modification of the Hammer technique (Covey et al. 2007) to a set of spectra from the LAMOST pilot survey, obtaining a sample of 67,000 M dwarfs.

Another analysis has been carried out by Z15, and it is this sample that we will use as a foundation for our study. Z15

selected a large sample of M giants and M dwarfs from LAMOST DR1 using a template fitting method to select M-type stars. They find over 100,000 spectra that show the characteristic molecular titanium oxide (TiO), vanadium oxide (VO), and calcium hydride (CaH) features typical of M-type stars. They then take this sample and calculate the TiO5, CaH2, and CaH3 spectral indices. The TiO and CaH spectral indices were defined by Reid et al. (1995) and Lépine et al. (2007), and the distribution of the spectral indices is a good indicator to separate M dwarf stars with different metallicity (Gizis 1997; Lépine et al. 2003, 2007, 2013; Mann et al. 2012). Figure 1 in Z15 shows the distribution of identified M-type stars in the TiO5 against CaH2+CaH3 plot. The M giants generally have weaker CaH molecular bands for a given range of TiO5 values, which is also consistent with the giant/dwarf discrimination of Mann et al. (2012). We note that the spectral index distribution of M-type stars can be used to separate giants from dwarfs with little contamination, especially for late-type M giants.

The analysis of Z15 resulted in two catalogs, one containing 8639 M giant candidates and one with around 100,000 M dwarf candidates. It is these samples that we use in the following study. We augment these with a further catalog of 4000 spectroscopically confirmed QSOs from LAMOST DR1, in order to assess QSO contamination.

3. PHOTOMETRIC SELECTION OF M GIANTS

3.1. WISE and 2MASS Photometric Data

With these relatively pure spectroscopically identified M giants, M dwarfs, and QSO candidates selected from LAMOST DR1, we now attempt to find effective selection criteria for M giants using near- and mid-IR photometry.

The *Wide-field Infrared Survey Explorer* (WISE) is a medium-class space *Explorer* mission funded by NASA and launched in 2009 December. The WISE project mapped the whole sky in four bands ($W1$, $W2$, $W3$, and $W4$), centered at wavelengths of 3.4, 4.6, 12, and 22 μm (Wright et al. 2010).

We cross-matched our LAMOST sample of M giants, M dwarfs, and QSOs to the ALLWISE Source Catalog in the NASA/IPAC Infrared Science Archive, using a search radius of 3". More than 99% of the matched objects had LAMOST-WISE source separations less than 1". We also applied the following cuts to ensure high-quality data: $cc_{\text{flags}} = 0000$; $ext_{\text{flg}} = 0$; $W1_{\text{sigmpro}}$ and $W2_{\text{sigmpro}} < 0.05$, which means that the profile-fit photometric uncertainty is less than 0.05 mag; and finally three cuts to ensure that we avoid saturated photometry, $W1_{\text{sat}}$ and $W2_{\text{sat}} < 0.05$ (which means that the saturated pixel fraction is less than 0.05), and $W1 > 8.1$ mag (corresponding to the $W1$ saturation magnitude). After applying these quality cuts, we are left with 4136 M giants, 63,979 M dwarfs, and 644 QSOs with both LAMOST spectroscopy and WISE/2MASS photometry and 2MASS data. The mean photometric errors for our sample are $\delta J = 0.023$ mag, $\delta K = 0.024$ mag, $\delta W1 = 0.023$ mag, and $\delta W2 = 0.021$ mag.

Throughout we adopt the $E(B - V)$ maps of Schlegel et al. (1998), in combination with $A_r/E(B - V) = 2.285$ from Schlafly & Finkbeiner (2011) and $A_\lambda/A(r)$ from Davenport et al. (2014). This final conversion has a weak dependence on latitude (see Section 4.2 of their paper). In Appendix A we describe our implementation of this latitude dependence. For illustrative purposes, in the following figures we include an arrow denoting the reddening vector. For this we choose

$b = 30^\circ$, which corresponds to the value for high galactic latitudes. At high galactic latitudes the orientation of the reddening vector is independent of b ; at smaller latitudes the dependence means that in the $E(J - K)$ versus $E(W1 - W2)$ plane the reddening vector becomes closer to vertical as $|b|$ approaches 0. The length of the reddening vector in these figures corresponds to an extinction of $A_J = 0.5$ mag; this is around an order of magnitude larger than typical values at high latitudes, but underestimates the extinction at low latitudes (i.e., $|b| \lesssim 10^\circ$) and toward the central parts of the Galaxy.

3.2. Previous Selection Methods

In the past decades many studies have used M giants to trace substructures in the Milky way halo (e.g., Majewski et al. 2003; Rocha-Pinto et al. 2003; Yanny et al. 2009; Belokurov et al. 2014). One issue for these studies is the problem of contamination from M dwarfs, especially for samples derived from photometry. In this subsection we discuss previous methods that have been used to select M giants.

The simplest and most robust way to identify M giants is to use features in their spectra. In the optical band the main differences between giants and dwarfs can be seen in the morphology near the TiO band heads and also the lack of strong Na I absorption at 8200 Å. In the K band, giants possess significantly stronger CO bands than their dwarf counterparts (Bochanski et al. 2014). Another method, also based on spectroscopy, is to use the stellar parameters (such as effective temperature and surface gravity) to separate M giants. An example of this approach is shown in Figure 4 and Equation (2) of Belokurov et al. (2014), although in this example the temperature range they have selected is more commonly associated with K-type stars. This was a deliberate decision owing to issues with the reliability of the spectroscopic temperature estimation for M-type stars (V. Belokurov 2016, private communication). As we will show later in Section 3.3, 2MASS colors can be used to differentiate spectral class. The colors of stars from the Belokurov et al. selection ($0.7 \lesssim (J - K)_0 \lesssim 0.9$ mag) are consistent with early-type M giants, although some may be late-type K giants. Clearly the efficacy of this method relies on the accuracy of the measurements of temperature and gravity.

The above two methods both rely on spectroscopic data, but to efficiently map wide areas (and large volumes), it is often better to use photometric surveys. This can be done using optical data (e.g., Yanny et al. 2009), although better results have been achieved using NIR data, such as 2MASS (e.g., Majewski et al. 2003; Sharma et al. 2010; Bochanski et al. 2014). Figure 1 shows the 2MASS color-color diagram for our sample of M giants, M dwarfs, and QSOs identified from LAMOST (see Section 2). The blue contours show the distribution of M giants (corresponding to 1σ and 2σ , i.e., containing 68.3% and 95.4% of the data), the red contours M dwarfs, and the green triangles QSOs. The black arrow shows an example reddening vector (see Section 3.1 for further details).

The stellar locus is clearly defined in this figure, but there is no obvious division between M giants and M dwarfs. Although the QSOs are offset from the stars, there is also significant overlap. In Majewski et al. (2003), they used $(J - K)_0 > 0.85$ to remove M dwarf contamination, and the black box in Figure 1 shows their final selection region. Although these color cuts remove many of the M dwarf and QSO

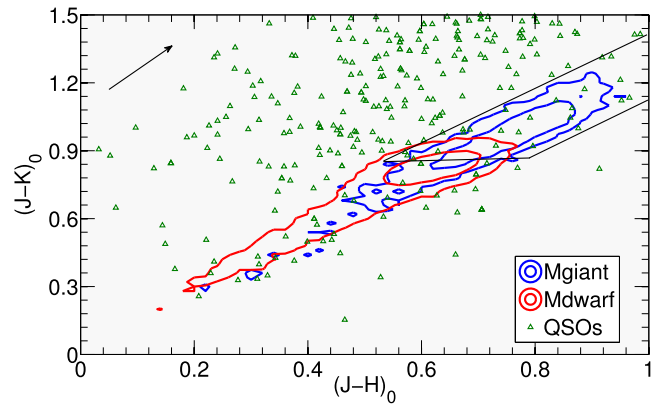


Figure 1. 2MASS $(J - K)_0$ vs. $(J - H)_0$ color-color distribution for spectroscopically classified M giants (blue contours), M dwarfs (red contours), and QSOs (green triangles). The contours correspond to 1σ and 2σ , i.e., they contain 68.3% and 95.4% of the data. The black arrow shows an example reddening vector (see Section 3.1 for further details), and the black box shows the Majewski et al. (2003) selection criteria.

contaminants, there are clearly still a significant number of M dwarfs present in this region. In Bochanski et al. (2014), they used a similar selection region, applying a stricter color cut of $(J - K)_0 > 1.02$ to remove more M dwarf contamination. This indeed removes more of the M dwarfs, but at a cost of removing many genuine M giants with $(J - K)_0 < 1.02$. After applying the Bochanski et al. (2014) color cuts to our spectroscopically classified sample, we find that these 2MASS-selected M giant candidates still have 13.5% dwarf contamination, and many M giants have been sacrificed (the M giant completeness is only 48.7%). Although these percentages will depend on the magnitude range under consideration and the underlying LAMOST selection function, they give an indication of the problems faced by these techniques. In short, by using NIR data it is not possible to entirely remove M dwarf contamination and simultaneously ensure reasonable levels of M giant completeness.

3.3. 2MASS and WISE Selection Criteria

A better way to identify M giants is to use mid-IR data, such as that available from the WISE mission. A combined 2MASS and WISE color-color diagram for M giants, M dwarfs, and QSOs is shown in Figure 2, where the data used here are the same as in Figure 1.

The separation of QSOs from stars is substantially improved, with the former having much redder $(W1 - W2)_0$ color. As before, the separation is not perfect, and a few QSOs appear to lie amid the stellar locus, particularly around $(J - K)_0 \approx 0.5$. Although most of these are low signal-to-noise ratio (S/N) spectra (almost all have $S/N < 10$) and hence are probably misclassified, around 20% or more appear to be binary stars composed of an M dwarf around a hotter companion.

From this figure one can also see that the $(J - K)_0$ versus $(W1 - W2)_0$ color-color plane enables a relatively clean separation of M giants from M dwarfs, much more efficiently than NIR data alone. There appear to be a small number of M giants located in M dwarf region, but these are actually misidentified M giants. For low-S/N spectra the dwarf/giant spectroscopic classification breaks down, and it becomes increasingly difficult to separate the two populations. If we

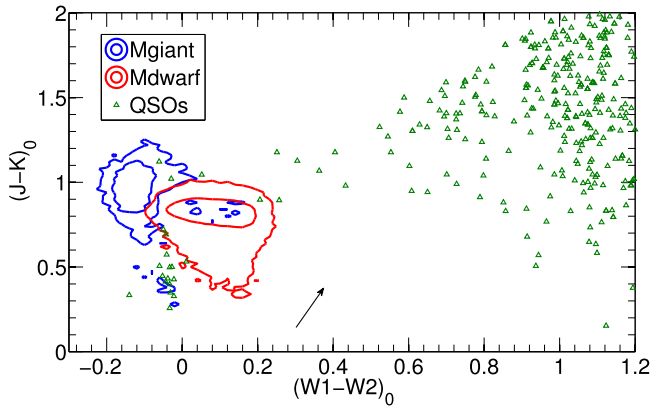


Figure 2. 2MASS and WISE $(J - K)_0$ vs. $(W1 - W2)_0$ color-color distribution for spectroscopically classified M giants (blue contours), M dwarfs (red contours), and QSOs (green triangles). The contours correspond to 1σ and 2σ . The black arrow shows an example reddening vector (see Section 3.1 for further details). There are a small number of M giants located in the M dwarf region, but these are most likely misclassified owing to having low-S/N spectra (see Section 3.3).

remove stars with low-S/N spectra (i.e., $S/N < 5$), then these spurious objects almost all disappear.

One issue that is not dealt with in Figure 2 is the properties of cooler stars, such as K dwarfs/giants. To address this, we have supplemented our data with a sample of LAMOST K-type stars from Liu et al. (2014), which have been classified using spectral line features. The distributions in the $(J - K)_0$ versus $(W1 - W2)_0$ plane are shown in Figure 3. There is an overlap between late K and early M giants, which is not surprising and most likely due to the Liu et al. sample including a number of early M giants, but reassuringly there is very little overlap between K dwarfs and M giants. This implies that a 2MASS–WISE color selection should be free from significant dwarf contamination.

Given these findings, we now define the following selection region for M giants:

$$\begin{aligned} -0.23 < (W1 - W2)_0 < 0.02, \\ 0.85 < (J - K)_0 < 1.3, \\ (J - K)_0 > 1.45 \times (W1 - W2)_0 + 1.05. \end{aligned} \quad (1)$$

This has been chosen to minimize contamination while retaining a reasonable level of completeness. Assuming that the spectroscopic classifications are reliable, we find that there is only 4.9% contamination from dwarfs in the color box given in Equation (1). Furthermore, we believe that most of this contamination is likely due to misclassified spectra; if we remove all spectra with S/N less than 10, then the contamination from dwarfs drops to less than 1%.

Any discussion of contamination and completeness will depend on the details of the selection function (e.g., the presence of color biases), the sky coverage, and the magnitude range under consideration, with brighter magnitudes containing a higher M giant/M dwarf fraction. This is because at bright magnitudes the volume probed by M dwarfs is small and at faint magnitudes the number of M giants drops because there are so few at large distances in the halo. For reference, the magnitude range probed by our sample is $7.63 \lesssim J_0 \lesssim 15.52$.

A similar approach was adopted by Koposov et al. (2015), although they chose a narrower selection region in the $(J - K)_0$ versus $(W1 - W2)_0$ color-color plane (see Equation

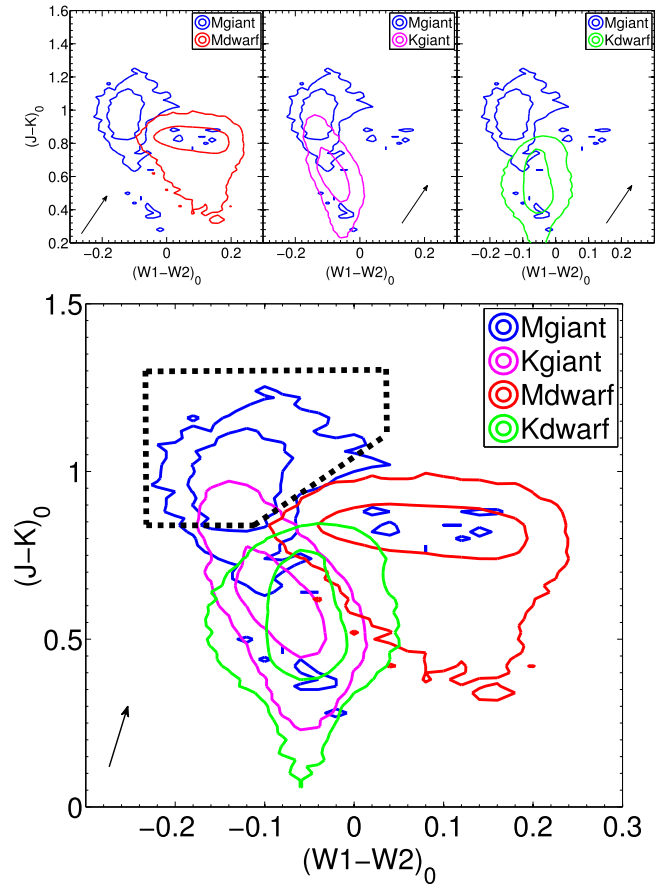


Figure 3. 2MASS and WISE $(J - K)_0$ vs. $(W1 - W2)_0$ color-color distribution for spectroscopically classified M giants (blue), M dwarfs (red), K giants (purple), and K dwarfs (green). Contours correspond to 1σ and 2σ . The dashed box shows our M giant selection criteria. The black arrow shows an example reddening vector (see Section 3.1 for further details).

(1) of their paper). The performance of their selection is comparable to ours; their completeness is around 10% lower owing to the narrower selection, and their contamination, while still below 5%, is slightly higher than ours since their selection is closer to the M dwarf region.

4. PROPERTIES OF M GIANTS

4.1. Metallicity Estimation

In Figure 3 we can see that most M giants are located in the region $(W1 - W2)_0 < -0.1$, but there is an extension to redder $(W1 - W2)_0$ colors. After checking the location of the stars that populate this extended region, we find that most of them are at high galactic latitudes, indicating that they are likely to be more metal-poor. This WISE metallicity trend is also predicted by stellar models, as can be seen (for example) in Figure 1 of Koposov et al. (2015).

To go one step further, we compare the photometry of our M giants to the spectroscopic metallicity obtained using data from the SDSS project APOGEE (Holtzman et al. 2015). This survey is taking high-S/N and high-resolution ($R = 22,500$) NIR spectra, resulting in detailed chemistry and a measurement of $[M/H]$ to a precision of better than 0.1 dex. We cross-match APOGEE DR12 with WISE and 2MASS, using the same photometric quality cuts as described in Section 3.1 with an additional cut of $|b| > 30^\circ$, and then use our photometric

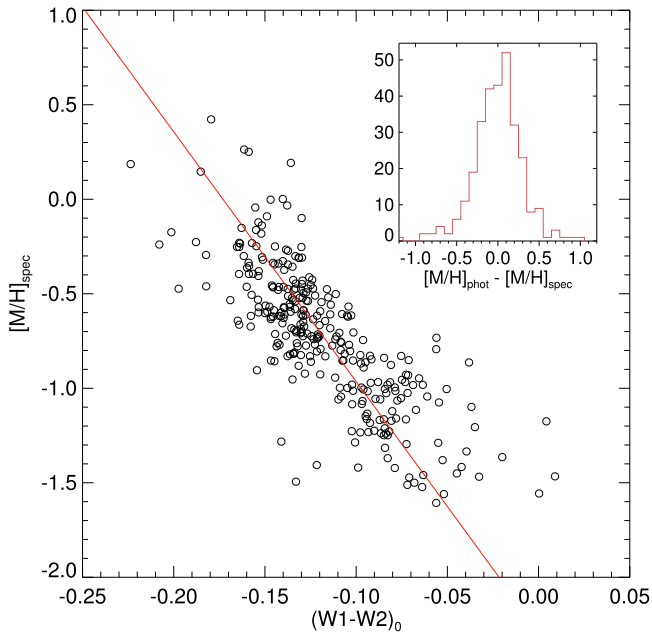


Figure 4. Metallicity distribution of APOGEE M giants vs. $(W1 - W2)_0$ color. The red line shows the best-fit linear relationship. The inset histogram shows the scatter in metallicity about this relation, which has a dispersion of 0.29 dex. Note that the mean error in $[M/H]_{\text{APOGEE}}$ is 0.03 dex and the mean error in $(W1 - W2)_0$ is 0.03 mag, which implies that the intrinsic scatter in this relation is exceptionally small (see Section 4.1).

criteria to select a sample of M giants. Figure 4 shows the APOGEE metallicities of the resulting sample of 296 M giants as a function of $(W1 - W2)_0$ color. The correlation with $(W1 - W2)_0$ is very strong and can be fit with the following linear relation:

$$[M/H]_{\text{phot}} = -13.2_{-0.6}^{+0.5} \times (W1 - W2)_0 - 2.28_{-0.07}^{+0.06} \text{ dex}, \quad (2)$$

taking into account errors on both color and metallicity (Hogg et al. 2010).

As can be seen from the inset of Figure 4, the residual scatter about this linear relation is small (0.29 dex). What is most remarkable about this is that the spread is almost entirely due to photometric uncertainties. The mean photometric error on $(W1 - W2)_0$ for these stars is 0.031 mag, which is larger than the measured spread in $(W1 - W2)_0$ about the linear relation (0.022 mag). This implies that the photometric uncertainties are probably overestimated and, in any case, the intrinsic dispersion in this relation must be exceptionally small. If we attempt to fit the relation including a term to represent the intrinsic spread (Equation (35) of Hogg et al. 2010), we find, as expected, that the best-fit spread is zero.

It should be noted that the APOGEE parameter pipeline encounters difficulties for very cool giants, with a recommendation that metallicities for stars cooler than 4000 K should be treated with caution (Holtzman et al. 2015). Around one-third of the members in our cross-matched sample are cooler than this limit, and so to check the effect on our relation, we repeat the fit excluding these stars. The resulting relation is very similar, although slightly steeper,

$$[M/H]_{\text{phot}} = -15.6_{-0.2}^{+0.4} \times (W1 - W2)_0 - 2.58_{-0.04}^{+0.06} \text{ dex}. \quad (3)$$

Throughout the paper we adopt the original relation (Equation (2)) and label these metallicities $[M/H]_{\text{phot}}$.

Clearly $(W1 - W2)_0$ is a very good proxy for $[M/H]$, meaning that this can be used to quantify metallicities of halo substructures (as we will demonstrate later in Section 5). Similar work has been carried out by Schlaufman & Casey (2014), finding that *WISE* photometry can efficiently identify metal-poor stars.

In Figure 5 we show the distribution of M giants on the sky, using our M giant selection from Equation (1) and photometric quality cuts as described in Section 3.1. We add a further cut of $J_0 > 12$, to ensure that our stars are beyond ~ 10 kpc, and $10.5 < W1_0 < 13.5$, which is optimal for detecting the Sgr stream. Using our photometric metallicity $[M/H]_{\text{phot}}$, we show two distributions in this figure: in the top panel we show all M giants, whereas in the bottom panel we show the more metal-poor ones (by removing stars with $(W1 - W2)_0 < -0.13$, corresponding to $[M/H]_{\text{phot}} > -0.56$ dex). As can be seen from the bottom panel, this cut reduces the number of disk M giants in the sample and also removes some relatively metal-rich substructures in the halo, such as the Tri-And system located at R.A. $\sim 30^\circ$, decl. $\sim 30^\circ$ (Majewski et al. 2004; Rocha-Pinto et al. 2004; see, e.g., Figure 7 of Deason et al. 2014 for a plot of the metallicity distribution).

4.2. Distance Estimation

4.2.1. An Empirical Distance Relation

In Figure 5, we can see the Sgr stream, LMC, and SMC very clearly. We can use these structures to estimate an M giant color–absolute magnitude relation, since we already know their distances. To do this, we first calculate the absolute magnitude (M_J) for each M giant in these regions using distance estimates from the literature, assuming that all stars lie at the systemic distance of the structure.

We select four regions from the top panel of Figure 5: a region near the core⁶ of Sgr ($285^\circ < \alpha < 300^\circ$, $-35^\circ < \delta < -28^\circ$; hereafter called the Sgr core region), one near the apocenter of the leading tail of Sgr ($214^\circ < \alpha < 226^\circ$, $-10^\circ < \delta < 0^\circ$), an LMC region ($60^\circ < \alpha < 105^\circ$, $-78^\circ < \delta < -60^\circ$), and an SMC region ($5^\circ < \alpha < 25^\circ$, $-77^\circ < \delta < -70^\circ$). The distances we adopted for the LMC, SMC, Sgr core, and Sgr leading apocenter are 51 kpc (Keller & Wood 2006; de Grijs et al. 2014), 61 kpc (Keller & Wood 2006), 29 kpc (calculated using the model of Law & Majewski 2010), and 53 kpc (Belokurov et al. 2014), respectively.

Figure 6 shows M_J versus $(J - K)_0$ relations in our four regions. As has been seen by many authors (e.g., Sharma et al. 2010), the absolute magnitude for M giants varies approximately linearly with $(J - K)_0$ color. However, it is not precisely linear, so we choose to fit these data using the following power-law relation:

$$M_{J,\text{fit}} = A_1 [(J - K)_0^{A_2} - 1] + A_3, \quad (4)$$

where A_3 corresponds to the value of M_J at $(J - K)_0 = 1$ mag. We do this by slicing the data into M_J segments and fitting each of these with two Gaussians (one for the system and one for the background). We then fit the

⁶ We have not included the actual Sgr core in order to avoid low-latitude regions where extinction and crowding could affect our analysis.

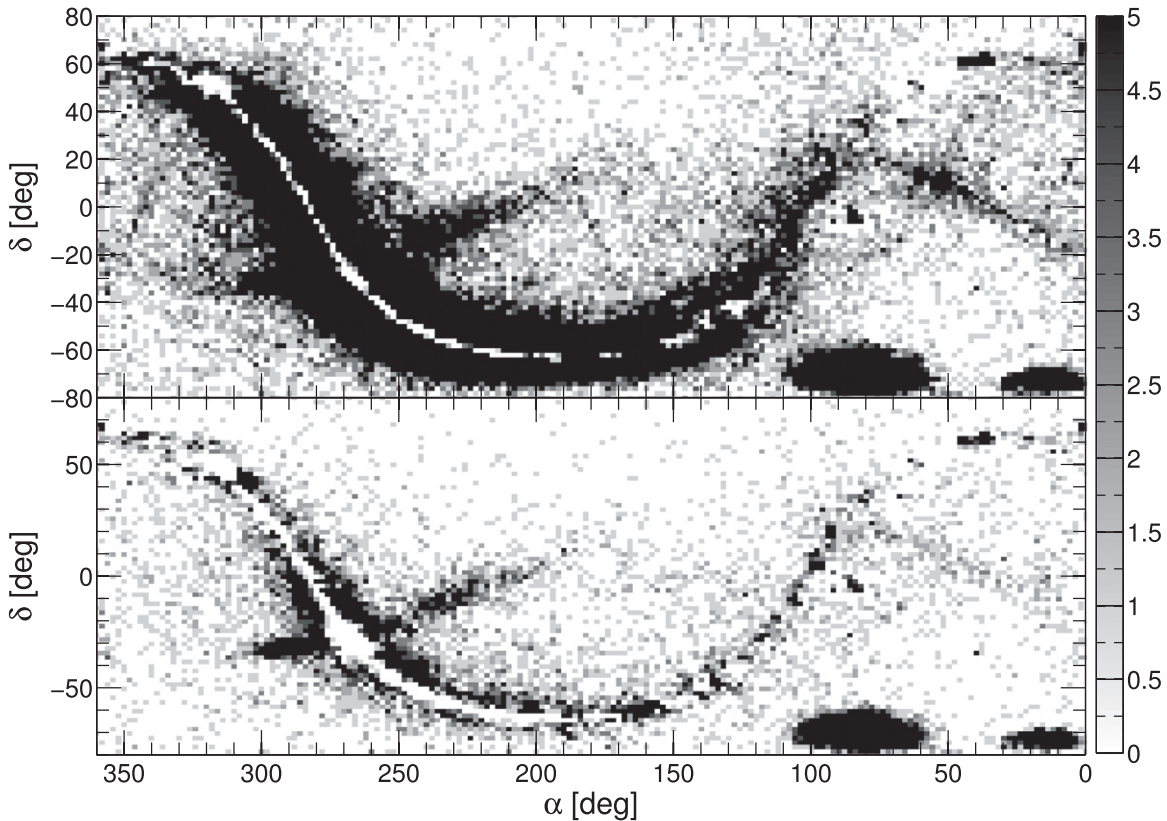


Figure 5. Full sky map of M giants. The top panel shows all M giants, and the bottom panel shows metal-poor M giants using the cut $(W1 - W2)_0 > -0.13$ mag (corresponding to $[M/H]_{\text{phot}} < -0.56$ dex). Note that this cut reduces the amount of disk M giants and also removes some relatively metal-rich substructures in the halo, such as the Tri-And system located at R.A. $\sim 30^\circ$, decl. $\sim 30^\circ$ (see Section 4.1).

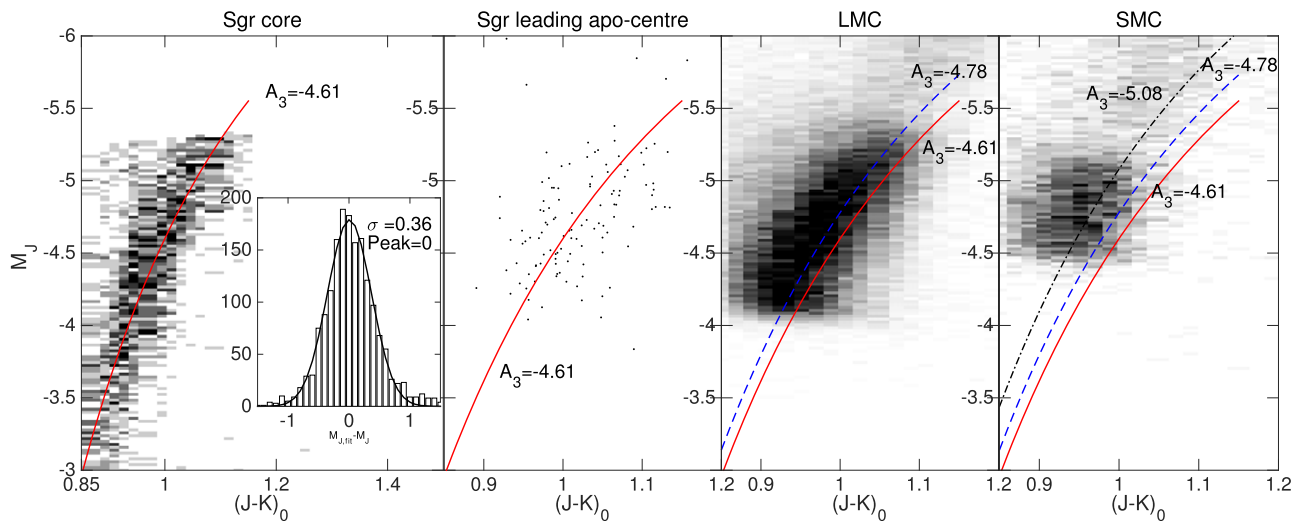


Figure 6. Color and J -band absolute magnitude relation for four separate regions: Sgr core, Sgr leading apocenter, LMC, and SMC. We calculate M_J assuming that all stars lie at the systemic distance of the respective structure (taking literature values for these distances; see Section 4.2). The value of A_3 corresponds to the offset in absolute magnitude between these relations (Equation (4)). The solid line denotes the best fit to the Sgr core, the dashed line to the LMC, and the dot-dashed line to the SMC.

centroids of the former Gaussians with the above polynomial relation.

We start with the Sgr core region, which covers the largest magnitude range (owing to the fact that it is the closest of the three structures). The parameters are presented in Table 1 and

should be valid for the color range that we probe, i.e., $0.9 \lesssim (J - K)_0 \lesssim 1.1$. The inset in the first panel of Figure 6 shows the scatter around the $M_{J,\text{fit}}$ relationship. The dispersion is 0.36 mag, which corresponds to a distance uncertainty of 20%. Note that this uncertainty does not take into account

Table 1

The Parameters for Our Color–Absolute Magnitude Relation ($M_{J,\text{fit}}$), as Given in Equation (4)

Region	A_1	A_2	A_3
Sgr core	3.12	-2.6	-4.61
LMC	-4.78
SMC	-5.08

Note. For the Sgr core region all three parameters are left free. For the other two regions only A_3 is free and the remaining parameters are fixed to the values found for the Sgr core. These relations should be valid for $(J - K)_0$ in the range 0.9–1.1 mag.

population effects (which we discuss next), and so this estimate can be considered as a lower limit on the actual uncertainty.

In the second panel of Figure 6 we compare the Sgr core fit to data from the leading tail’s apocenter, finding very good agreement. The final two panels of this figure show the derived relation for the LMC and SMC, where we have kept parameters A_1 and A_2 fixed to match the Sgr core values. As expected, the color–absolute magnitude relation varies between Sgr and the LMC and SMC, owing to the different metallicities and star formation histories of these systems. Figure 7 shows the metallicity distribution function (MDF) in these four regions, using the photometric metallicity relation presented in Equation (2). It is interesting to note that although the MDFs for the Sgr core and SMC are quite similar, their $M_{J,\text{fit}}$ relations vary significantly. In fact, despite having a significant shift in mean metallicity compared to the Sgr core, the LMC has a much better agreement in terms of $M_{J,\text{fit}}$. These discrepancies are likely caused by the different star formation histories in these systems. This can also be seen when one considers the difference between the Sgr core and leading apocenter regions, which have very similar $M_{J,\text{fit}}$ relations yet clearly discrepant MDFs. This is most likely a consequence of the fact that the leading apocenter material is composed of stars stripped from the outer parts of the infalling dwarf, while the core material is from the younger populations in the center. So the shift in $M_{J,\text{fit}}$ from the MDF offset is probably canceled by a corresponding shift coming from the age offset. We return to the issue of Sgr in Section 5.

We performed the following simple test to check whether internal extinction in these systems is likely to be affecting our derived $M_{J,\text{fit}}$ relations. We took two LMC samples, one consisting of the entire LMC region ($60^\circ < \alpha < 105^\circ$, $-78^\circ < \delta < -60^\circ$) and one covering the same area but excluding the central region ($70^\circ < \alpha < 90^\circ$, $-72^\circ < \delta < -68^\circ$), where internal extinction will be most significant. We then performed the same $M_{J,\text{fit}}$ fitting to these two regions and found that there was no clear shift in the relations, confirming that internal extinction is unlikely to bias our results.

In Figure 8 we compare our $M_{J,\text{fit}}$ relation to some of those in the literature. The two main references we use are Sharma et al. (2010) and Sheffield et al. (2014). The former paper uses a single linear relation calibrated to match a range of stellar models with ages and metallicities consistent with simulated stellar halos (Bullock & Johnston 2005). Sheffield et al. (2014) generalized this to include a metallicity dependence, again using stellar models. For completeness we also include the relation from Covey et al. (2007), which the authors admit is not especially robust (this relation is itself based on Pickles [1998], who use solar-age and solar-abundance stellar models).

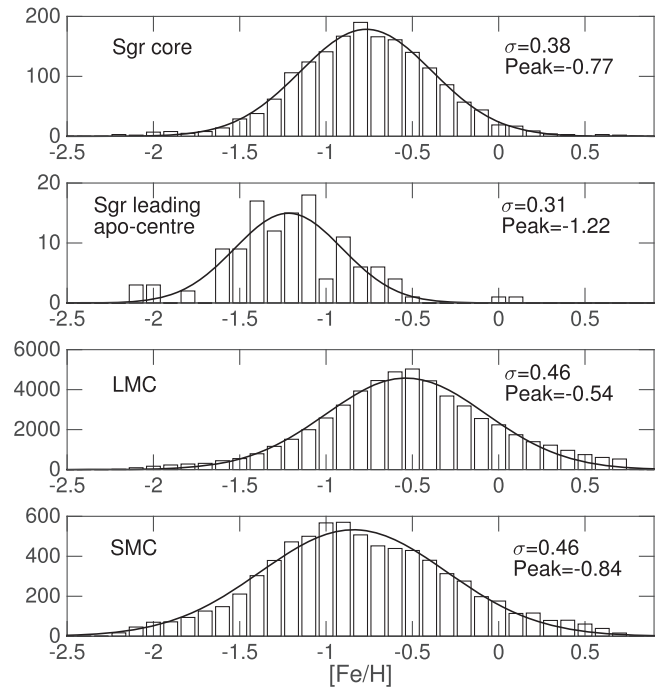


Figure 7. Photometric $[\text{Fe}/\text{H}]$ distribution in the Sgr core, Sgr apocenter, LMC, and SMC regions, as derived from Equation (2).

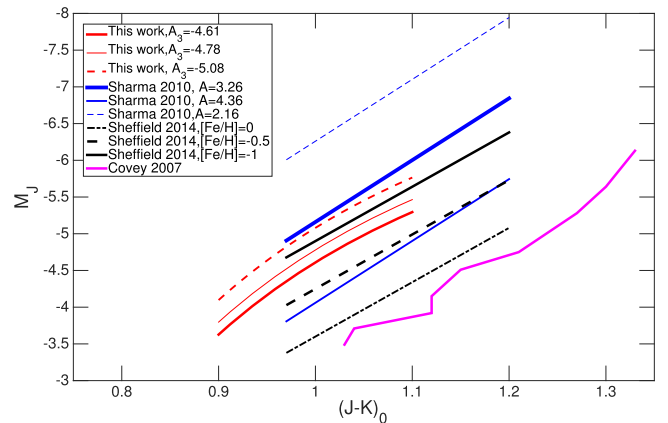


Figure 8. Comparison of our empirical distance relation to various literature sources. The red lines correspond to our new relations, where the top, middle, and bottom lines correspond to relations based on the SMC, LMC, and Sgr, respectively. Our relations are only valid for the range $0.9 \lesssim (J - K)_0 \lesssim 1.1$, while the Sharma et al. and Sheffield et al. ones are valid for $0.97 \lesssim (J - K)_0 \lesssim 1.2$.

Note that our method differs from these in that it is an empirical relation, rather than relying on stellar models. We can see that our three relations (Sgr, LMC, and SMC) are consistent with the $[\text{Fe}/\text{H}] = 0$ relation from Sheffield et al. (2014), even though these three systems are all more metal-poor than this value. In particular, our Sgr relation, which provides a good match to the leading apocenter where $[\text{Fe}/\text{H}] \lesssim -1$, is offset from Sheffield et al.’s $[\text{Fe}/\text{H}] = -1$ relation by around 1 mag. As discussed above, this may be due to the age dependence of these relations. We conclude that a simple relation based on metallicity might overlook some subtleties and hence not be ideal for all purposes.

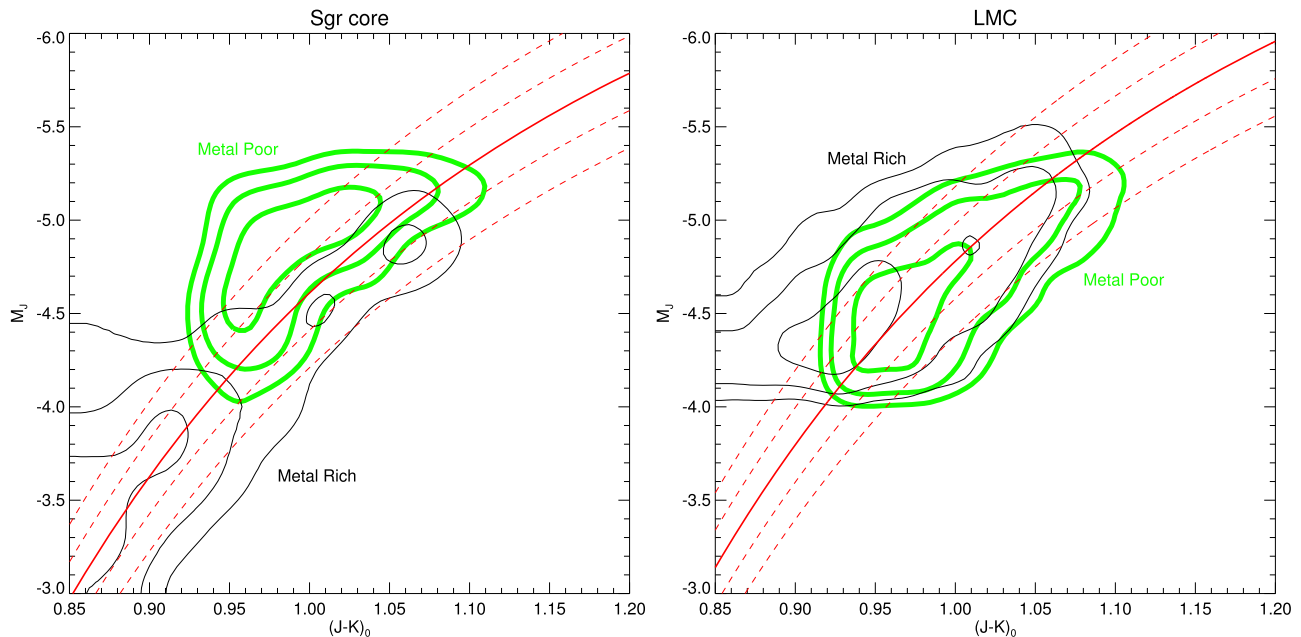


Figure 9. The dependence of our derived M_J vs. $(J - K)_0$ relation on metallicity. The thick contours show a sample of stars that are 0.5 dex more metal-poor than the overall population, while the thin contours show a sample that is 0.5 dex more metal-rich. Contours correspond to 0.3, 0.5, and 0.8 times the peak value. The solid line denotes the fiducial relation derived in Section 4.2.1, and the dashed lines correspond to ± 0.2 and ± 0.4 mag in M_J .

4.2.2. Metallicity Dependence and Age–Metallicity Trends in the LMC and Sagittarius

The location of the RGB in color–magnitude space is well known to be dependent on both age and metallicity. Given the metallicity relation found in the previous section, the question naturally arises whether we can detect metallicity gradients within our distance relation.

We first test the core region of Sgr, where we have the most coverage of the color–magnitude plane. We repeat the same procedure as above, assuming that all stars lie at a distance of 29 kpc, but for two samples: one with metallicity around 0.5 dex greater than the mean and one around 0.5 dex smaller ($-0.42 < [M/H] < 0.00$ dex and $-1.50 < [M/H] < -1.12$ dex, respectively, where the mean photometric metallicity is -0.76 dex). In order to clean the sample, in each band we reject the stars with 10% largest photometric errors. The two samples have around 250 stars each.

The resulting distributions of M_J versus $(J - K)_0$ are shown in Figure 9. The fiducial relation derived for the whole population (Section 4.2.1) is shown by the solid red line. As can be seen, especially for the region $0.95 < (J - K)_0 < 1.10$ mag, there is a systematic shift with the metal-rich population lying below the relation and the metal-poor one above. This matches the expectation from stellar models, where for a given age metal-poor populations are bluer. The dashed lines in this figure correspond to the fiducial relation shifted vertically by ± 0.2 and ± 0.4 mag, which means that the shift with metallicity for Sgr is around $0.3\text{--}0.6$ mag dex $^{-1}$.

It can also be seen that the metal-rich population extends to smaller $(J - K)_0$ colors. This is due to our diagonal color cut, which means that at redder $(W1 - W2)_0$ colors the M giant selection box does not extend as far in $(J - K)_0$ (see Figure 3).

We repeat this exercise for the LMC, where we have the largest number of M giants. We again reject lower-quality photometry, this time removing the stars with 20% largest photometric errors in each band. Our two metallicity ranges were again chosen to be 0.5

dex above and below the mean value ($-0.20 < [M/H] < -0.05$ dex and $-1.20 < [M/H] < -1.07$ dex, respectively, where the mean photometric metallicity is -0.63 dex). Each sample has around 2500 stars.

The resulting distributions, shown in Figure 9, are significantly different from those of Sgr. There is no clear trend with metallicity, and one might even claim that the metal-rich population is bluer than the metal-poor one. The contrasting behavior for the LMC and Sgr can be understood when one considers the difference between the star formation histories of these two systems. We know that the LMC retains gas and has an extended star formation history. As a consequence, the metal-rich populations are likely to be significantly younger than the metal-poor ones, which can lead to the M_J dependence on metallicity being canceled out. This is because the RGB for younger populations is generally bluer than older populations. However, the star formation history of Sgr is likely to be less extended than the LMC, as its infall into the Milky Way will have removed most of the gas and truncated star formation (see, e.g., de Boer et al. 2015).

4.2.3. Test Case: The Tilt of the LMC

Although the distance uncertainty for an individual M giant is relatively large (around 20% before considering population effects), for structures like the LMC we can average large numbers of stars to determine the distance to relatively high precision. We therefore test the performance of our relation by addressing the tilt in the LMC disk, which has been established by previous authors (e.g., Subramanian & Subramanian 2013, and references therein).

We do this by calculating M_J for each of the stars, assuming a distance of 51 kpc, and compare the distribution of magnitudes to the fiducial relation calculated above (see Table 1). The tilt means that stars on the near side will be on average brighter, while those on the far side will be on average fainter. Since we expect such variations to be correlated with azimuth, we divide up the data

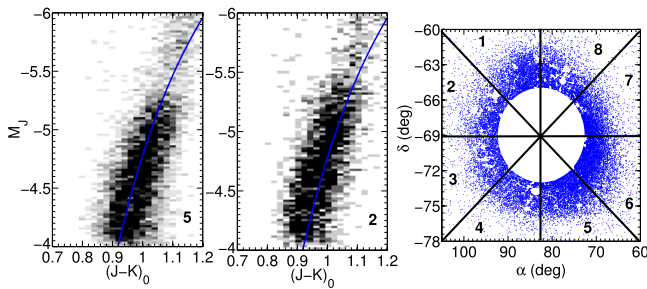


Figure 10. Our determination of the tilt of the LMC. We divide our data into eight azimuthal segments (right panel) and for each of these plot the color–absolute magnitude distribution assuming a systemic distance of 51 kpc. The left and middle panels show segments 2 and 5, which are the closest and most distant segments, respectively. The solid line denotes the fiducial relation calculated in Table 1. There are clear distance offsets in these regions, reflecting the fact that the LMC is tilted to our line of sight. Note that we have excluded the inner regions as we do not expect that these will exhibit significant tilt.

into eight segments, as shown in the right panel of Figure 10. The central regions will exhibit negligible tilt, so we exclude these using an ellipse with major axis of 10° and minor axis of 4° , centered on $(\alpha, \delta) = (83^\circ, -69^\circ)$. The left and middle panels show the color–absolute magnitude relation for two of these segments, compared to the fiducial relation. There are clear magnitude offsets in some of these regions, with Segment 2 (middle panel) hosting stars that are on average brighter than the fiducial relation, while Segment 5 (left panel) shows the opposite behavior. To quantify this discrepancy, we calculate the mean offset from the fiducial relation for each numbered segment by fitting the distribution with a Gaussian function. The results are presented in Table 2. From this we can see that the offsets exhibit a clear sinusoidal behavior with azimuth, as expected if the LMC is tilted to our line of sight. By fitting a sine curve to these offsets (excluding Segment 7, which has an unusually broad M giant branch and does not match the overall trend), we find that the position angle of the line of nodes is $128^\circ.5$, where the angle is measured eastward from the north. This compares favorably to Subramanian & Subramanian (2013), who found an angle of $141^\circ.5$.

We can also investigate the inclination angle, but this is slightly harder to measure as it is also a function of the distance of the stars from the center of the LMC. The amplitude of the offsets in Table 2 is around 0.11 mag, and the separation of these stars is around 10° from the center of the LMC. This corresponds to an inclination of around 16° , which is not too dissimilar from the value of $25^\circ.7$ found by Subramanian & Subramanian (2013).

5. MAPPING THE SAGITTARIUS STREAM

In Figure 5 we have shown the distribution of M giants across the entire sky. The most prominent features in this figure are the LMC and SMC (located in the bottom right corner of each panel), but in addition the Sgr stream is clearly visible, extending from the core of the dwarf galaxy located behind the Galactic bulge (lying at R.A. = 284° and decl. = -30°). This map is qualitatively similar to that obtained from 2MASS M giants (Majewski et al. 2003), but as we have shown above, our version will have less M dwarf contamination.⁷ There are

⁷ Our map is very similar to that of Koposov et al. (2015, right panel of Figure 2), owing to the fact that our 2MASS and *WISE* selection cuts are similar to theirs (see Section 3.3).

Table 2

The Values of the Mean Offset in *J*-band Magnitude as a Function of Azimuth for Eight Segments around the LMC

Segment	Mean Offset (mag)
1	−0.151
2	−0.184
3	−0.101
4	0.004
5	0.029
6	0.021
7	−0.192
8	−0.121

Note. The segment number corresponds to those in Figure 10.

further stream-like detections (e.g., at R.A., decl. = $180^\circ, -10^\circ$ or $90^\circ, -20^\circ$), but these are most likely artifacts due to the *WISE* scanning law. We present a table of all M giants from this map in Appendix B (Table 4).

5.1. Distances to the Stream

Given the relations obtained in the previous section, we now proceed to analyze the distribution of Sgr M giants. We start off by looking at the heliocentric distances to the stream. This is shown in the bottom panel of Figure 11, where we have plotted all M giants obtained using the selection criteria defined in Equation (1) but restricted ourselves to only those stars that lie within 10° of the Sgr orbital plane (defined following the equations in the Appendix of Belokurov et al. 2014; note that this coordinate system is related to the Majewski et al. [2003] system through $\tilde{\Lambda} = 360 - \Lambda$ and $\tilde{B} = -B$). Distances have been calculated using the Sgr relation given in Section 4.2. Background subtraction has been performed by averaging two fields at $10^\circ < \tilde{B} < 20^\circ$ and $-20^\circ < \tilde{B} < -10^\circ$. We have omitted the two regions closest to the bulge ($\tilde{\Lambda} < 40^\circ$ and $\tilde{\Lambda} > 320^\circ$) as confusion means that it is difficult to reliably identify the Sgr stream.

This plot clearly shows the leading stream reaching apocenter at around 50–60 kpc at $\tilde{\Lambda} = 50^\circ$ – 60° and the trailing stream at $\tilde{\Lambda} > 220^\circ$. We see good agreement with literature distances (shown by the solid black lines in this panel; taken from Belokurov et al. 2014), although there is a possible discrepancy in the gradient for the leading debris around $\tilde{\Lambda} \gtrsim 100^\circ$, which may be due to population effects affecting our distance relation. This may occur if the material more distant from the core is more metal-poor or older, having been stripped earlier. We return to the issue of metallicities later in this section. It is worthwhile to note that although these literature distances come from a variety of tracers (blue horizontal branch stars, red clump stars, subgiant branch stars, and now M giants), the agreement is remarkably consistent.

There has been recent controversy over the potential detection of the apocenter of the trailing tail of the Sgr stream by Belokurov et al. (2014), based on blue horizontal branch stars and kinematics of giant stars in SDSS (see also Newberg et al. 2003; Drake et al. 2013). This detection is shown with the distant black line in the bottom panel of Figure 11. Recent evidence to support this claim comes from Koposov et al. (2015), where they take velocities of M giants around $\tilde{\Lambda} \sim 200^\circ$ – 230° and find good agreement between the existing

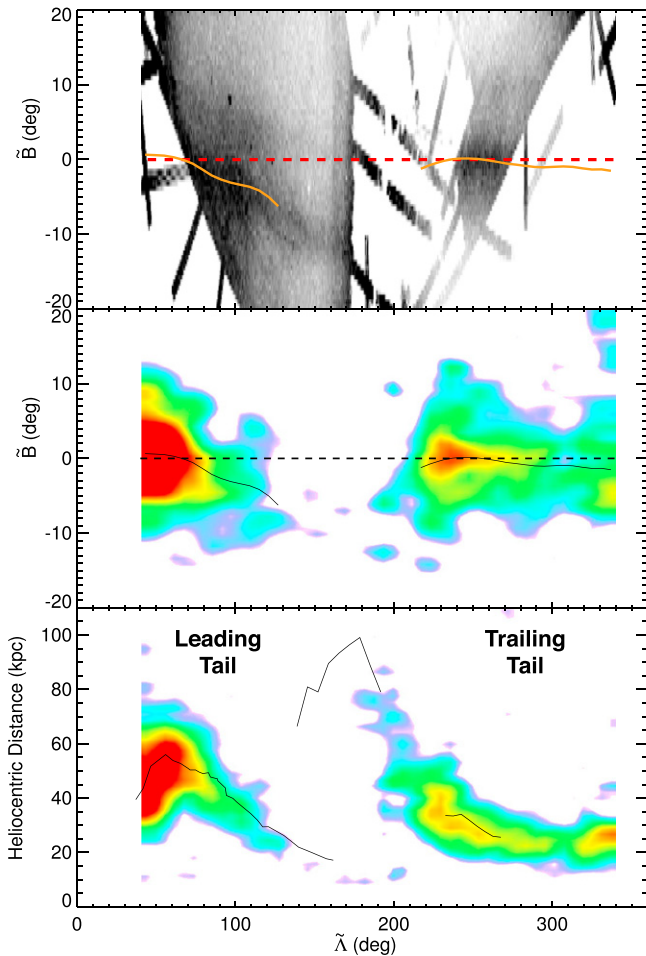


Figure 11. Sagittarius stream tomography and distance. The middle panel shows the density of our *WISE*-selected M giants in the Sgr coordinate system (see the Appendix of Belokurov et al. 2014). In this system the Sgr dwarf is located at $(0, 0)$ and its orbit moves in the direction of increasing $\tilde{\Lambda}$. We have only included stars that have distances within 10 kpc of the stream. The centroid of the stream is denoted by the solid line. The top panel shows the equivalent plot for MSTO stars (taken from Koposov et al. 2012), and the solid line is the same as the middle panel. The bottom panel shows heliocentric distance measurements of our *WISE*-selected M giants for $-10^\circ < \tilde{B} < 10^\circ$. Solid lines show detections from Belokurov et al. (2014), consisting of subgiant branch, RGB, and blue horizontal branch detections.

trailing debris and the proposed apocenter detection. Making a detection of this connecting material is difficult owing to the fact that at this point the stream passes through the disk in the Galactic anticenter. However, given the purity of the giant sample from our *WISE* selection, we are also able to support the hypothesis that the distant detection is the apocenter of the trailing tail. Although the *WISE* data are not deep enough to reach the apocenter itself, in the bottom panel of Figure 11 we clearly detect a bridge of stars connecting the well-studied trailing material at $\tilde{\Lambda} > 210^\circ$ with the apocenter detection at $\tilde{\Lambda} < 190^\circ$. If one takes all M giants in this region ($180^\circ < \tilde{\Lambda} < 210^\circ$ and $55 < D_{\text{helio}} < 80$ kpc), there is an overdensity around the plane of the stream (with $\tilde{B} \sim 5^\circ$).

Belokurov et al. (2014) also argued that the trailing stream may extend even further, connecting to an overdensity located around $\tilde{\Lambda} \sim 110^\circ$ (which is sometimes referred to as Branch C; see Belokurov et al. 2006; Correnti et al. 2010). We also find a tentative detection of this overdensity (with around 10–15 M giants; this is the weak spur at $\tilde{\Lambda} = 115^\circ$ and at a distance

of 45 kpc in Figure 11), implying that its existence is robust as it has been detected in samples of subgiants, red clump stars, and now M giants. It is indeed clustered around the Sgr orbital plane, but appears to be relatively broad (with $-15^\circ \lesssim \tilde{B} \lesssim 5^\circ$). One may expect the stream to be more diffuse this far from the core. However, until one can detect material connecting Branch C to the apocenter detection (which is not evident in our data), its nature remains up for debate.

5.2. Orbital Plane

In the middle panel of Figure 11 we have plotted the distribution of Sgr stream stars on the sky, rotated into the Sgr coordinate system (Belokurov et al. 2014). In this system Sgr lies at $(0, 0)$ and its orbit moves in the direction of increasing $\tilde{\Lambda}$. To construct this figure, we have only included M giants within 10 kpc of the stream (as given by the black lines in the bottom panel, where we have linearly extrapolated for the regions with no detections). We have also incorporated a background subtraction, averaging two regions on either side of this range (i.e., $20^\circ \lesssim \tilde{B} \lesssim 30^\circ$ and $-30^\circ \lesssim \tilde{B} \lesssim -20^\circ$) and interpolating between them.

As mentioned above, it is difficult to determine the behavior toward the anticenter ($\tilde{\Lambda} \sim 180^\circ$), but apart from that the stream is clearly detected and lies close to the adopted stream plane (i.e., $\tilde{B} = 0$). We have fit the cross-stream profile with a Gaussian model in order to trace the centroid of the density distribution, and this is shown by the two solid lines. The trailing tail lies almost precisely on the orbital plane. The leading stream, however, shows clear deviation from the plane and crosses at a shallow angle. This offset between the orbital planes of the leading and trailing tails is not new; for example, Johnston et al. (2005) did this with 2MASS M giants, finding an offset of around 5° – 10° in the orientation of the two poles. More recent studies have been carried out by Newby et al. (2013) and Belokurov et al. (2014).

In order to interpret this plot, we now compare this to the behavior of main-sequence turnoff (MSTO) stars in this region. Many authors have looked at the distribution of MSTO stars, and we have included a map of MSTO density in the top panel of Figure 11 (taken⁸ from Koposov et al. 2012). The MSTO stars exhibit the well-known “bifurcation” in the leading stream, splitting into two separate branches bisected by $\tilde{B} = 0$ with the faint companion stream at $\tilde{B} \sim 2^\circ$. Koposov et al. (2012) also detect a bifurcation in MSTO stars in the trailing stream, with the bifurcation being harder to detect and consisting of a faint wing to the distribution (around $-15^\circ < \tilde{B} < 5^\circ$; see also Slater et al. 2013).

Our distributions (also shown by the solid lines in the top panel) show good agreement with the bright MSTO stream in both the leading and trailing tails, but with no evidence for a bifurcation. The location where the bifurcation is clearest in MSTO stars is around $100^\circ < \tilde{\Lambda} < 160^\circ$, but here the density of M giants is low, and so it is hard to detect even the bright stream. Therefore, this nondetection may be because there are insufficient stars to sample the faint secondary stream, or this may be due to physical differences between the two streams. There are two main hypotheses for the origin of the faint stream: either this is material from an earlier wrap of the stream

⁸ Note that there is an error in the axis labeling of Figure 1 in Koposov et al. (2012), as the B axis has the wrong sign. See Figure 2 of Belokurov et al. (2014) for a correct version.

(e.g., de Boer et al. 2015), or this is from a smaller companion system to the main progenitor (e.g., Koposov et al. 2012). Both of these scenarios are consistent with our nondetection of the faint stream, if one argues that the faint stream should possess fewer M giants as it is older and more metal-poor than the bright stream (because the faint stream contains material stripped from the outer parts of the progenitor where there is less metal enrichment, or because it is simply from a smaller system with less metal enrichment). One final point to note is that Koposov et al. (2012) claimed to detect a bifurcation in the distribution of 2MASS-selected M giants in the trailing tail, with the faint stream lying at $5^\circ < \tilde{B} < 10^\circ$ for $240^\circ < \tilde{\Lambda} < 270^\circ$. We, however, are unable to confirm this with our *WISE*-selected sample.

Our detection shows very good agreement with the bright stream, although the leading tail appears to be misaligned by a couple of degrees. This could be due to statistical fluctuations, especially if a few M giants from the faint stream were biasing the centroid fits. The other explanation is that this offset is due to population effects, as one would not necessarily expect the M giants and MSTO stars to share the same radial profile in the progenitor system. Rather, we expect that the M giants, which are rare in halo populations, should be more tightly bound and centrally concentrated than the MSTO stars, and this may lead to the two populations being stripped differently and hence not lying on identical orbital planes. We defer a detailed analysis of the alignment of the orbital planes to a further study. An in-depth discussion of the alignment and precession of the stream has been presented in Belokurov et al. (2014), which compares the orbital plane of the MSTO and red clump stars to that of the M giants as measured by Johnston et al. (2005). They also find that the M giants lie close to the plane of the bright stream, with the orbital poles being a few degrees offset for the leading stream and almost identical for the trailing stream.

5.3. Metallicity Gradient

In Section 4.1 we demonstrated that the *WISE* *W1* and *W2* bands provide a very good measure of an M giant’s metallicity. Given this fact, we now investigate the metallicity gradient in the stream. Previous attempts to do so have been published, but are usually limited to small sample sizes or are drawn from inhomogeneous populations (e.g., Chou et al. 2007, 2010; Monaco et al. 2007; Keller et al. 2010). Using our photometric relation, we are able to estimate metallicities for a large number of stars, all belonging to the same population (i.e., M giants).

We have measured the metallicity distribution at two locations along the stream, as shown in Figure 12. Here we have restricted ourselves to only plotting stars with $-10^\circ < \tilde{B} < 10^\circ$ and (as in the previous subsection) those whose distances are within 10 kpc of the stream. Although our photometric metallicity relation is valid over a large range ($-1.5 \lesssim [\text{Fe}/\text{H}] \lesssim 0$ dex), values beyond this should be treated with caution; this is because our linear relation is based on APOGEE data, which only cover $-1.5 \lesssim [\text{Fe}/\text{H}] \lesssim 0$ dex, and so values beyond this are based on extrapolations. As discussed in Section 4.1, the uncertainty in this relation is 0.22 dex.

From Figure 12 we can see a clear offset between the two streams, with the leading stream being more metal-poor. This is in good agreement with the result in Monaco et al. (2007, see their Figure 7), albeit with an order of magnitude more stars. Our measurement of the trailing tail metallicity is also in good

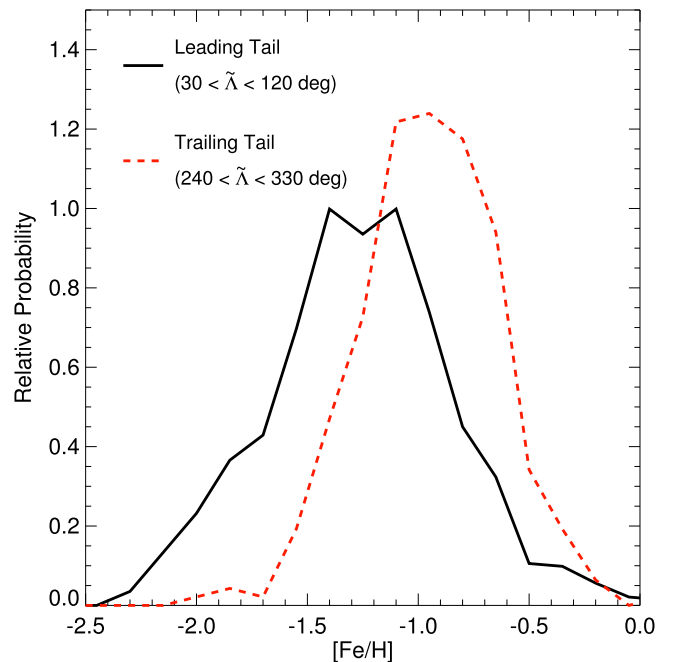


Figure 12. Metallicity distributions for leading ($30 < \tilde{\Lambda} < 120$; solid) and trailing ($240 < \tilde{\Lambda} < 330$; dashed) tails of the Sagittarius stream, estimated using the *WISE* M giant metallicity relation defined in Section 4.1. This plot only uses stars that are at $-10 < \tilde{B} < 10$ and have distances within 10 kpc of the stream.

agreement with that derived from MSTO stars in Carlin et al. (2012). The mean and standard deviations of our distributions are $(-1.00, 0.43)$ and $(-0.88, 0.31)$ dex for the leading and trailing streams, respectively. Since the uncertainty in the photometric metallicity relation is around 0.2 dex, the small dispersions indicate that there is little intrinsic spread in the M giant metallicity for each tail, especially for the trailing tail. Note that we were unable to find any significant gradients *within* the leading or trailing streams, probably owing to the lack of precision in the metallicity measurements.

Such an offset between the two streams can be explained by internal metallicity gradients in the progenitor dwarf. If the outer regions are more metal-poor, then the fact that these will be stripped earlier than the inner regions sets up a metallicity gradient along the stream. Although our leading and trailing metallicity distributions are both measured around 100° from the core, they actually correspond to material stripped at different times. By analyzing the Sgr disruption history from the model of Law & Majewski (2010), we find that our trailing material is predicted to consist of debris stripped during the most recent pericentric passage, while our leading material includes debris stripped from the last two pericentric passages (see Figure 17 of Law & Majewski 2010). This naturally leads to the observed offset in metallicity (and also explains the narrower dispersion in metallicity for the trailing tail), from which we can conclude that the progenitor dwarf must have been massive enough to support internal metallicity gradients.

One may wonder whether our distributions are affected by interlopers from the aforementioned Tri-And system. However, if we minimize potential Tri-And contamination by avoiding $20^\circ < \text{RA} < 60^\circ$ (Deason et al. 2014), then our findings remain unchanged, indicating that this structure is not strongly biasing our results. Contamination from foreground M dwarfs could also affect our results, but if we reduce potential

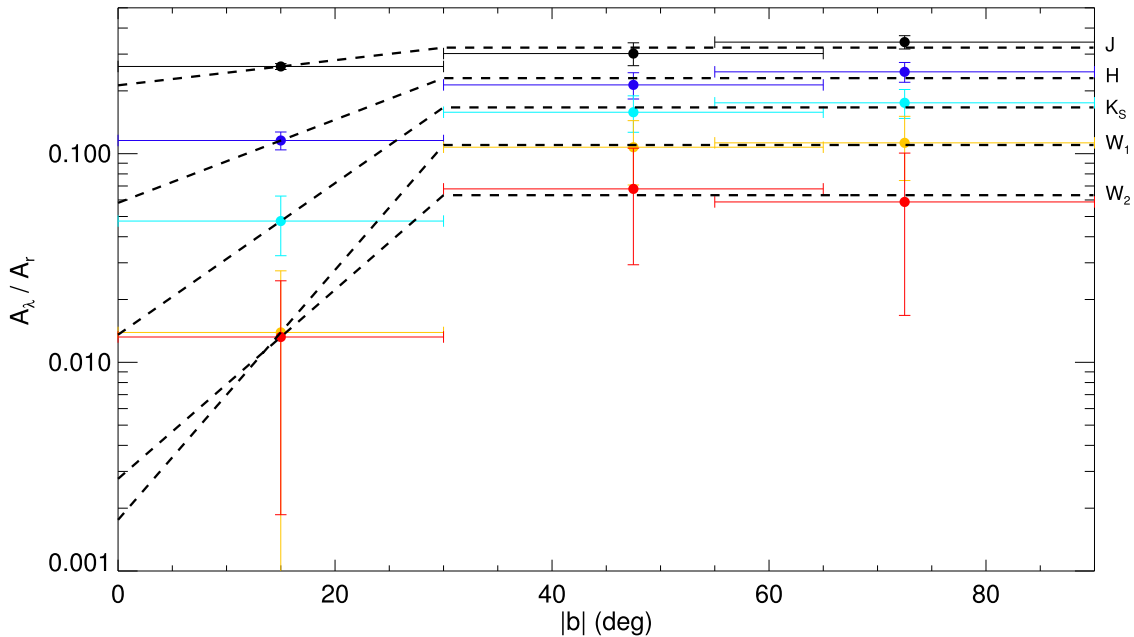


Figure 13. Our latitude-dependent extinction law derived from the data of Davenport et al. (2014). The horizontal error bars denote the range of b used for that data point.

contamination by employing a stricter $(J - K)_0$ cut of 0.95 mag (see Figure 3), our findings are unchanged.

6. CONCLUSIONS

We have shown that *WISE*+2MASS photometry can be used to efficiently identify M giant stars. By using a large sample of spectroscopically confirmed M giants from LAMOST, we have devised a photometric selection (Equation (1)) that contains only a few percent dwarf contamination and negligible contribution from QSOs. At fainter magnitudes the dwarf contamination will increase, but as we have shown in Section 3, this method is far superior to those constructed using 2MASS photometry alone.

We have also constructed new photometric distance relations, using large samples of M giants from known structures (e.g., LMC/SMC/Sgr). The variations in these distance relations reflect the differing chemical composition of these structures. Unlike most previous attempts to define distance relations, our approach is entirely empirical and does not rely on stellar models. We have demonstrated the accuracy of these relations by investigating the tilt of the LMC. The fact that we are able to reproduce the previously detected tilt shows that when averaging over large samples of M giants, these relations can be used to obtain precise distances.

As has been noted previously (e.g., Schlafman & Casey 2014; Koposov et al. 2015), the *WISE* IR bands are sensitive to a star’s metallicity. Using the high-S/N, high-resolution spectroscopic metallicities from APOGEE, we found a strong correlation between the $(W1 - W2)_0$ color and $[M/H]$. This is well fit by a linear relation (Equation (2)), with a scatter of 0.35 dex. The most remarkable aspect of this is that the scatter in $(W1 - W2)_0$ is comparable to the observational error in the photometry, implying that the intrinsic dispersion in this relation must be exceptionally small. This means that it is possible to quickly amass large samples of M giants that are (a) free from dwarf contamination and (b) have good metallicity

Table 3
Values of the Parameters in Our Latitude-dependent Extinction Law (Equation (5)), Derived from the Data of Davenport et al. (2014)

λ	m	c
<i>J</i>	0.0060	0.3223
<i>H</i>	0.0199	0.2302
<i>K</i>	0.0363	0.1666
<i>W1</i>	0.0599	0.1100
<i>W2</i>	0.0453	0.0633

estimates, without having to undertake time-consuming spectroscopic observations.

We applied our photometric selection criteria to the ALLWISE catalog to obtain a large sample of stars from the Sgr stream. Using the above distance and metallicity relations, we then investigated the properties of the stream. We confirmed that the plane of the orbit is misaligned for the leading and trailing tails, as is the case for the MSTO population. The recent detection of Sgr debris toward the Galactic anticenter (Koposov et al. 2015) was confirmed, and although the *WISE* data do not allow us to detect the recently identified apocenter of the trailing tail (Belokurov et al. 2014), the anticenter material clearly forms a bridge between the known trailing tail and the proposed apocenter detection. The proposed Branch C of the stream can also be seen in our M giant sample, and, despite being relatively tentative, the fact that it has been seen in a range of tracers (subgiants, red clump stars, and now M giants) means that it is unlikely to be spurious. However, we are unable to confirm that Branch C is an extension of the trailing tail as we find no stars connecting this to the trailing apocenter material.

Our photometric metallicity relation also allowed us to investigate the metallicity of the stream. Using a large sample of stars from a homogeneous population alleviates biases inherent when using a variety of different tracer populations.

Table 4
Table of Positions, Magnitudes, and Reddening for a Sample of Halo M Giants

ALLWISE ID	R.A. (degree)	decl. (degree)	J (mag)	δJ (mag)	K (mag)	δK (mag)	$W1$ (mag)	$\delta W1$ (mag)	$W2$ (mag)	$\delta W2$ (mag)	$E(B - V)$ (mag)
J010035.43-021511.8	15.1476612	-2.2532981	14.637	0.067	13.469	0.057	13.048	0.033	13.068	0.039	0.0367
J024752.75-003735.2	41.9698317	-0.6264614	13.944	0.026	13.018	0.034	12.914	0.024	13.019	0.031	0.0356

(This table is available in its entirety in machine-readable form.)

The offset between the leading and trailing material can be clearly seen (Figure 12) and is around 0.2 dex. The fact that there is an offset is consistent with prediction from the model of Law & Majewski (2010), as our leading material sample consists of debris stripped in the last two pericentric passages, while our trailing sample consists only of debris stripped in the most recent pericentric passage. There can now be no doubt that the progenitor system must have been massive, containing a significant radial metallicity gradient; otherwise, such metallicity offsets would not be present along the stream.

M giants are a valuable resource for studying our Galaxy. Their bright absolute magnitudes mean that they can be used to trace distant structures in the disk and halo. In future work we will investigate the disk population, studying low-latitude substructures or the truncation of the stellar disk. A more complete picture can be inferred when radial velocities are incorporated into the analysis. For example, the first data release of the LAMOST survey contains almost 10,000 M giant spectra, which we are now in the process of analyzing. This will be especially important for dissecting low-latitude substructures, but will also allow us to confirm the nature of Sgr Branch C and potentially detect new halo overdensities. As well as substructures, M giant velocities can be used to study the global properties of the Milky Way, for example, constraining the mass profile of the halo.

The authors wish to thank Sergey Koposov and Vasily Belokurov for their input into this study. We are also indebted to James R. A. Davenport for providing the extinction data from Figure 8 of Davenport et al. (2014). We wish to thank the referee, whose comments helped improve the clarity of the work.

This work was supported by the following grants: the 973 Program 2014 CB845702/2014CB845700; the Strategic Priority Research Program “The Emergence of Cosmological Structures” of the Chinese Academy of Sciences (CAS, grant XDB09010100); the CAS One Hundred Talent fund; and the National Natural Science Foundation of China (NSFC) under grants 11173002, 11333003, 11373054, 11073038, 11073001, 11373010, and 11390373. J.L.C. and H.J.N. acknowledge support from the U.S. National Science Foundation under grants AST 09-37523 and AST 14-09421.

Z.J. would like to acknowledge the National Natural Science Foundation of China (NSFC, Grant No. 11503066) and the Shanghai Natural Science Foundation (14ZR1446900).

The Guoshoujing Telescope (LAMOST) is a National Major Scientific Project built by the CAS. Funding for the project has been provided by the National Development and Reform Commission. LAMOST is operated and managed by the National Astronomical Observatories, CAS.

This publication makes use of data products from the *Wide-field Infrared Survey Explorer*, which is a joint project of the University of California, Los Angeles, and the Jet Propulsion

Laboratory/California Institute of Technology, funded by the National Aeronautics and Space Administration.

APPENDIX A EXTINCTION CORRECTION

Since many of our M giants are at low latitudes, we need to carefully take extinction into account. Recent work by Davenport et al. (2014) has shown that at near- and mid-infrared bands the dust extinction law varies as a function of Galactic latitude. This can result in up to an order-of-magnitude difference in A_λ/A_r when comparing high to low latitudes.

We account for this latitude dependence using a simple prescription. Taking the data from Figure 8 of Davenport et al. (2014), we fit the extinction law for each band using a constant value for $|b| > 30^\circ$ and a power law for $|b| < 30^\circ$,

$$\begin{aligned} A_\lambda/A_r &= c \, 10^{m(|b|-30)} \text{ for } |b| < 30^\circ \\ A_\lambda/A_r &= c \text{ for } |b| \geq 30^\circ. \end{aligned} \quad (5)$$

The resulting fits are shown in Figure 13, and the values of m and c are given in Table 3. Throughout the paper we correct for extinction using Equation (5).

APPENDIX B TABLE OF HALO M GIANTS

Here we present a table of halo M giants. These have been selected using the photometric quality cuts described in Section 3.1 and the M giant classification from Equation (1). We impose a further cut $J_0 > 12$ mag, to ensure that our stars are at distances of greater than ~ 10 kpc, hence removing nearby disk stars. Distances for these stars can be calculated using Equation (4), metallicities using Equation (2), and extinctions using Equation (5). Values of $E(B - V)$ are derived from the maps of Schlegel et al. (1998). This table must be used with caution at low latitudes, since source confusion and problems with the extinction maps (e.g., the low resolution) can affect the reliability of the sample.

REFERENCES

- Belokurov, V., Koposov, S. E., Evans, N. W., et al. 2014, *MNRAS*, 437, 116
 Belokurov, V., Zucker, D. B., Evans, N. W., et al. 2006, *ApJL*, 642, L137
 Bochanski, J. J., Willman, B., West, A. A., Strader, J., & Chomiuk, L. 2014, *AJ*, 147, 76
 Bonaca, A., Geha, M., & Kallivayalil, N. 2012, *ApJL*, 760, L6
 Bressan, A., Marigo, P., Giradi, L., et al. 2012, *MNRAS*, 427, 127
 Bullock, J., & Johnston, K. V. 2005, *ApJ*, 635, 931
 Cardelli, J. A., Clayton, G. C., & Mathis, J. S. 1989, *ApJ*, 345, 245
 Carlin, J. L., Majewski, S. R., Casetti-Dinescu, D. I., et al. 2012, *ApJ*, 744, 25
 Chou, M.-Y., Cunha, K., Majewski, S. R., et al. 2010, *ApJ*, 708, 1290
 Chou, M.-Y., Majewski, S. R., Cunha, K., et al. 2007, *ApJ*, 670, 346
 Correnti, M., Bellazzini, M., Ibata, R. A., et al. 2010, *ApJ*, 721, 329
 Covey, K. R., Ivezić, Ž., Schlegel, D., et al. 2007, *AJ*, 134, 2398
 Davenport, J. R. A., Ivezić, Ž., Becker, A. C., et al. 2014, *MNRAS*, 440, 3430
 Deason, A. J., Belokurov, V., Hamren, K. M., et al. 2014, *MNRAS*, 444, 3975

- de Boer, T. J. L., Belokurov, V., & Koposov, S. 2015, *MNRAS*, **451**, 3489
- de Grijs, R., Wicker, J. E., & Bono, G. 2014, *AJ*, **147**, 122
- Deng, L.-C., Newberg, H. J., Liu, C., et al. 2012, *RAA*, **12**, 735
- Drake, A. J., Catelan, M., Djorgovski, S. G., et al. 2013, *ApJ*, **765**, 154
- Gizis, J. E. 1997, *AJ*, **113**, 806
- Hogg, D. W., Bovy, J., & Lang, D. 2010, arXiv:1008.4686
- Holtzman, J. A., Shetrone, M., Johnson, J. A., et al. 2015, *AJ*, **150**, 148
- Johnston, K. V., Law, D. R., & Majewski, S. R. 2005, *ApJ*, **619**, 800
- Keller, S. C., & Wood, P. R. 2006, *ApJ*, **642**, 834
- Keller, S. C., Yong, D., & Da Costa, G. S. 2010, *ApJ*, **720**, 940
- Koposov, S. E., Belokurov, V., Evans, N. W., et al. 2012, *ApJ*, **750**, 80
- Koposov, S. E., Belokurov, V., Zucker, D. B., et al. 2015, *MNRAS*, **446**, 3110
- Law, D. R., & Majewski, S. R. 2010, *ApJ*, **714**, 229
- Lépine, S., Hilton, E. J., Mann, A. W., et al. 2013, *AJ*, **145**, 102
- Lépine, S., Rich, R. M., & Shara, M. M. 2003, *AJ*, **125**, 1598
- Lépine, S., Rich, R. M., & Shara, M. M. 2007, *ApJ*, **669**, 1235
- Liu, C., Deng, L.-C., Carlin, J. L., et al. 2014, *ApJ*, **790**, 110
- Luo, A.-L., Zhao, Y.-H., Zhao, G., et al. 2015, *RAA*, **15**, 1095
- Majewski, S. R., Ostheimer, J. C., Rocha-Pinto, H. J., et al. 2004, *ApJ*, **615**, 738
- Majewski, S. R., Skrutskie, M. F., Weinberg, M. D., & Ostheimer, J. C. 2003, *ApJ*, **599**, 1082
- Mann, A. W., Brewer, J. M., Gaidos, E., Lépine, S., & Hilton, E. J. 2013, *AJ*, **145**, 52
- Mann, A. W., Gaidos, E., Lépine, S., & Hilton, E. J. 2012, *ApJ*, **753**, 90
- Monaco, L., Bellazzini, M., Bonifacio, P., et al. 2007, *A&A*, **464**, 201
- Newberg, H. J., Yanny, B., Grebel, E. K., et al. 2003, *ApJL*, **596**, L191
- Newberg, H. J., Yanny, B., Rockosi, C., et al. 2002, *ApJ*, **569**, 245
- Newberg, H. J., Yanny, B., & Willett, B. A. 2009, *ApJL*, **700**, L61
- Newby, M., Cole, N., Newberg, H. J., et al. 2013, *AJ*, **145**, 163
- Peth, M. A., Ross, N. P., & Schneider, D. P. 2011, *AJ*, **141**, 105
- Pickles, A. J. 1998, *PASPj*, **110**, 863
- Reid, I. N., Hawley, S. L., & Gizis, J. E. 1995, *AJ*, **110**, 1838
- Rocha-Pinto, H. J., Majewski, S. R., Skrutskie, M. F., & Crane, J. D. 2003, *ApJL*, **594**, L115
- Rocha-Pinto, H. J., Majewski, S. R., Skrutskie, M. F., Crane, J. D., & Patterson, R. J. 2004, *ApJ*, **615**, 732
- Schlafly, E. F., & Finkbeiner, D. P. 2011, *ApJ*, **737**, 103
- Schlaufman, K. C., & Casey, A. R. 2014, *ApJ*, **797**, 13
- Schlaufman, K. C., Rockosi, C. M., Lee, Y. S., et al. 2012, *ApJ*, **749**, 77
- Schlegel, D. J., Finkbeiner, D. P., & Davis, M. 1998, *ApJ*, **500**, 525
- Sharma, S., Bharathi, A., Chandra, S., et al. 2010, *PhRvB*, **81**, 174512
- Sheffield, A. A., Johnston, K. V., Majewski, S. R., et al. 2014, *ApJ*, **793**, 62
- Slater, C. T., Bell, E. F., Schlafly, E. F., et al. 2013, *ApJ*, **762**, 6
- Smith, M. C., Evans, N. W., Belokurov, V., et al. 2009, *MNRAS*, **399**, 1223
- Subramanian, S., & Subramaniam, A. 2013, *A&A*, **552**, AA144
- Wright, E. L., Eisenhardt, P. R. M., Mainzer, A. K., et al. 2010, *AJ*, **140**, 1868
- Yanny, B., Newberg, H. J., Johnson, J. A., et al. 2009, *ApJ*, **700**, 1282
- Yi, Z., Luo, A., Song, Y., et al. 2014, *AJ*, **147**, 33
- Zhao, G., Zhao, Y.-H., Chu, Y.-Q., et al. 2012, *RAA*, **12**, 723
- Zhong, J., Lépine, S., Hou, J., et al. 2015a, *AJ*, **150**, 42
- Zhong, J., Lépine, S., Li, J., et al. 2015b, *RAA*, **15**, 1154